



**Surface acoustic wave diffraction driven mechanisms in microfluidic systems**

Journal:	<i>Lab on a Chip</i>
Manuscript ID	LC-ART-03-2018-000243.R1
Article Type:	Paper
Date Submitted by the Author:	19-Jun-2018
Complete List of Authors:	Fakhfour, Armaghan; Monash University, Mechanical Devendran, Citsabehsan; Monash University, Mechanical and Aerospace Engineering Albrecht, Thomas; Monash University Collins, David; Massachusetts Institute of Technology, ; Massachusetts Institute of Technology, Electrical Engineering, Biological Engineering Winkler, Andreas; IFW Dresden, Micro- and Nanostructures Schmidt, Hagen; IFW Dresden, Micro- and Nanostructures Neild, Adrian; Monash University,



Cite this: DOI: 10.1039/xxxxxxxxxx

## Surface acoustic wave diffraction driven mechanisms in microfluidic systems<sup>†</sup>

Armaghan Fakhfouri,<sup>a</sup> Citsabehsan Devendran,<sup>a</sup> Thomas Albrecht,<sup>b</sup> David J. Collins,<sup>cde</sup> Andreas Winkler,<sup>f</sup> Hagen Schmidt,<sup>f</sup> and Adrian Neild,<sup>\*a</sup>

Received Date

Accepted Date

DOI: 10.1039/xxxxxxxxxx

www.rsc.org/journalname

Acoustic forces arising from high-frequency surface acoustic waves (SAW) underpin an exciting range of promising techniques for non-contact manipulation of fluid and objects at micron scale. Despite increasing significance of SAW-driven technologies in microfluidics, the understanding of a broad range of phenomena occurring within an individual SAW system is limited. Acoustic effects including streaming and radiation force fields are often assumed to result from wave propagation in a simple planar fashion. The propagation patterns of a single SAW emanating from a finite-width source, however, cause a far richer range of physical effects. In this work, we seek a better understanding of the various effects arising from the incidence of a finite-width SAW beam propagating into a quiescent fluid. Through numerical and experimental verification, we present five distinct mechanisms within an individual system. These cause fluid swirling in two orthogonal planes, and particle trapping in two directions, as well as migration of particles in the direction of wave propagation. For a range of IDT aperture and channel dimensions, the relative importance of these mechanisms is evaluated.

### 1 Introduction

Manipulation of particles is key for tasks such as sorting, patterning and concentration within microfluidic chips. Manipulation can take place using passive physical features to give rise to hydrodynamic interaction which result in motion along fluid streamlines.<sup>1–4</sup> Alternatively, active methods employ external force fields, arising from magnetic,<sup>5,6</sup> dielectrophoretic (DEP),<sup>7,8</sup> optical<sup>9,10</sup> or acoustical<sup>11</sup> effects, to act on the suspended objects.

Ultrasonic excitation generates acoustic forces acting both on suspended matter and the fluid itself. In addition, the straightforward on-chip integration, non-contact and bio-compatible nature<sup>12</sup> of acoustic methods has made them particularly interesting for biologically oriented microfluidic systems.<sup>13–15</sup> Two

key approaches have been established, the use of bulk acoustic waves<sup>16–18</sup> (BAW) and surface acoustic waves<sup>19–22</sup> (SAW). In BAW systems, a piezoelectric component which is adhered to the microfluidic chip is used as an excitation source. Waves couple into the fluid, which is typically contained within materials such as silicon and glass, in which strong reflections occur. By choice of a suitable excitation field, the resulting standing wave will become resonant, yielding sufficient forces to push particles to the planes of either the pressure nodes or antinodes. This means that the pressure field is restricted to the resonant modes of the fluid volume.<sup>23–26</sup>

SAWs are excited by a pair of comb-shaped electrodes on a piezoelectric substrate. By selecting a suitable frequency of oscillation, the waves which propagate from each electrode along the surface of the substrate interfere constructively. As the resonance required to maximise the amplitudes of excitation occurs due to this constructive interference, the frequency of operation is dictated by the pattern and spacing of the electrodes and not the fluid volume dimensions. Thus, it is not necessary to include interfaces which ensure high degrees of reflection; typical SAW systems use a fluid volume contained in polydimethylsiloxane (PDMS), a material which has lower acoustic impedance to that of water. Accordingly, a travelling surface acoustic wave<sup>27</sup> (TSAW) can be excited, where acoustic energy passes through the fluid and into the PDMS bulk, in which it is then damped. In contrast, standing surface acoustic waves<sup>28,29</sup> (SSAW) can be

<sup>a</sup> Laboratory for Micro Systems, Department of Mechanical and Aerospace Engineering, Monash University, Clayton, Victoria 3800, Australia.

<sup>b</sup> Department of Mechanical and Aerospace Engineering, Monash University, Clayton, Victoria 3800, Australia.

<sup>c</sup> Pillar of Engineering Product Development, Singapore University of Technology and Design, Singapore 487372, Singapore.

<sup>d</sup> Department of Biological Engineering, Massachusetts Institute of Technology, Cambridge, Massachusetts 02139, USA.

<sup>e</sup> Department of Electrical Engineering and Computer Science, Massachusetts Institute of Technology, Cambridge, MA 02139, USA.

<sup>f</sup> SAWLab Saxony, IFW Dresden, Dresden, D-01069 Germany

<sup>†</sup> Electronic Supplementary Information (ESI) available: [details of any supplementary information available should be included here]. See DOI: 10.1039/b000000x/

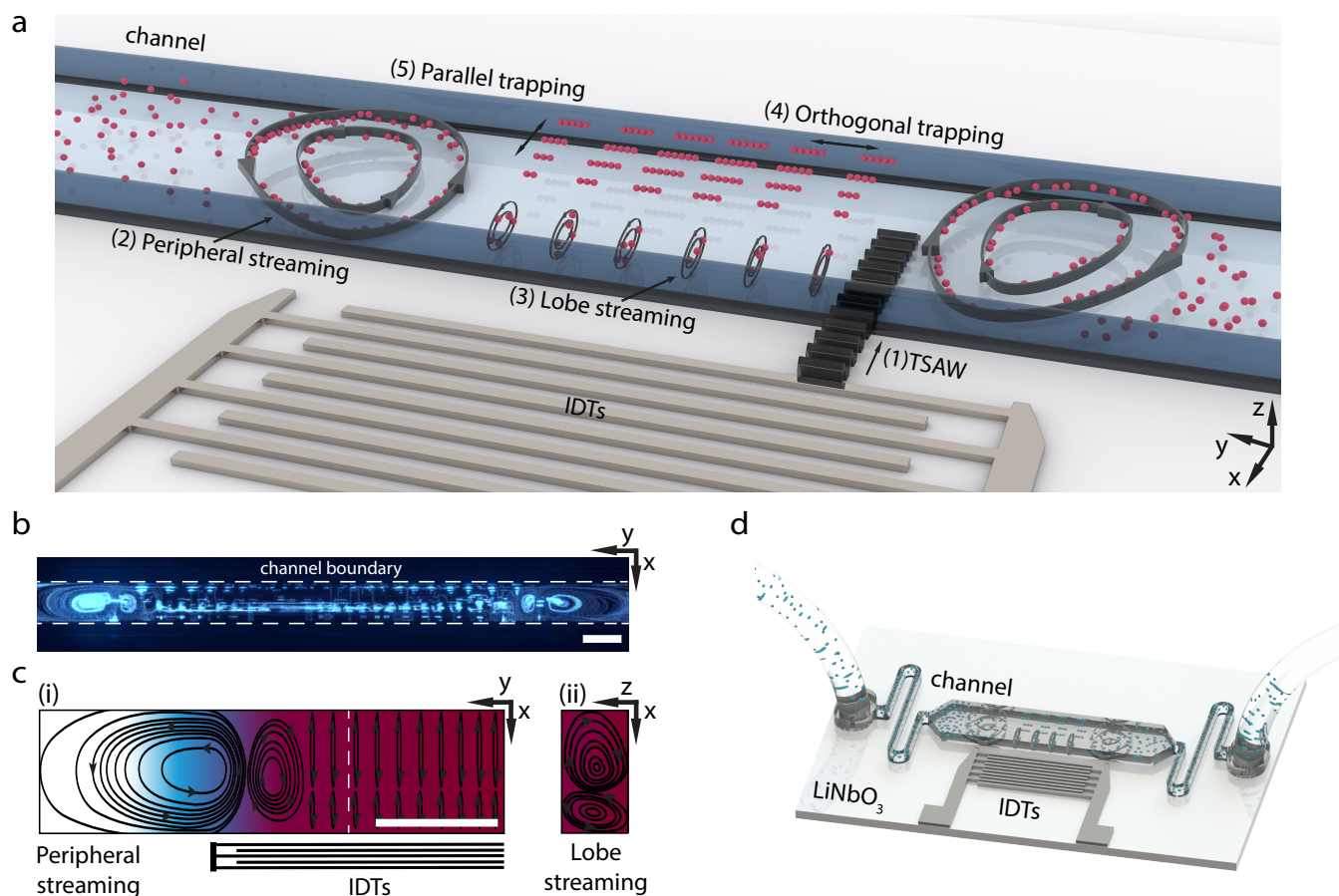


**Fig. 1** Visualisation of the combined acoustic streaming field and acoustic radiation force resulting from incidence of fluid and a TSAW generated by a finite-width set of IDT. (a) Conceptual illustration of particle behaviour upon interaction with the SAW-field depicting five distinct key mechanisms; (1) migration of particles in the direction of TSAW propagation, (2) peripheral streaming vortex ( $x$ - $y$  plane) at the SAW beam's edges, (3) lobe streaming vortices ( $x$ - $z$  plane) within the extent of SAW beam, (4) orthogonal trapping of particles along the  $y$ -direction due to diffraction patterns on the oscillating LN substrate along the TSAW propagation, (5) parallel trapping of particles (along the  $x$ -direction) as a result of diffraction in the fluid arising from the knife edge at the far end. (b) The mechanisms are experimentally visualized within an aqueous quiescent solution of  $1\ \mu\text{m}$  polystyrene particles subjected to a TSAW. (c) Streamlines of the acoustic streaming field generated by the TSAW-beam. Within (i-top view) the red region indicates high acoustic intensity which decreases as the colour fades to blue, and subsequently white (minimum intensity). The vertical vortices in the  $x$ - $z$  plane shown in (ii-cross-sectional view) are extracted from the dashed white lines in fig (i). (d) 3D rendered image of the experimental setup depicting key resultant mechanisms. Scale bars are  $100\ \mu\text{m}$

excited by the use of counter-propagating TSAWs. SAW-driven systems have found applications in droplet generation,<sup>30</sup> merging,<sup>31</sup> steering<sup>32</sup> and splitting,<sup>33</sup> atomization,<sup>34,35</sup> particle patterning,<sup>36,37</sup> size-based sorting<sup>38–40</sup> and filtration.<sup>41</sup>

Ultrasonic manipulation of particles requires the use of steady state forces, these arise through two main mechanisms. The propagation of a sound field in a fluid results in body forces being exerted on the fluid, giving rise to acoustic streaming,<sup>42–44</sup> where the resulting circulating flows entrain suspended particles.<sup>45,46</sup> The ultrasonic field also generates acoustic radiation forces<sup>47</sup> (ARF) which act directly on the suspended matter. The force field in a travelling wave copoupled into the fluid, pushes particles in the direction of wave propagation,<sup>48</sup> whilst in a standing wave particles are pushed towards pressure nodes<sup>49</sup> or antinodes<sup>50</sup> depending on the acoustic contrast of the suspended particle in a given surrounding medium. As the force profiles are different for each mechanism, establishing the dominant force is key

to understanding the resulting behaviour. In the case of BAW systems, the sound field has been modelled,<sup>51–54</sup> the streaming flows predicted,<sup>44–46</sup> and the size dependent nature of the force dominance has been described; there being a minimum particle size above which collection occurs within the standing wave.<sup>44</sup>

However, the complexity of SAW systems is still being elucidated. For example, a recent study examined the dominant force affecting particle behaviour outcomes in a SSAW, showing that the dominant effect is both size and location dependant;<sup>45</sup> this location dependence is not present in BAW. In addition, many recent studies, have added depth to the approximations made about SAW-driven microfluidics and challenged some of the assumptions commonly made. Firstly, in TSAW systems it is assumed that particles migrate away from the ultrasonic source. However, through a series of experiments, Destgeer *et al* showed that an anechoic corner exists in which no migration of particles is observed.<sup>55–57</sup> Secondly, diffraction of the ultrasonic wave aris-

ing from a discontinuity introduced by the channel wall, means that particles can be held in spatial periodic patterns within a TSAW system,<sup>58,59</sup> whereas the periodic nature of this outcome is usually only expected for SSAW excitation. Thirdly, the counter-propagation of two waves excited by separate sets of electrodes need not lead to standing waves and so periodic patterning. Rather, it can result in a single, movable, trapping location if two slightly different frequencies are used.<sup>60</sup> Finally, the distinction between SSAW and TSAW systems has been challenged, with the attenuation of each counter-propagating TSAW (used to establish a SSAW) meaning that different parts of a channel can be dominated by TSAW or SSAW, a fact that yields an accurate sorting mechanism.<sup>61</sup>

In light of these developments, which have highlighted the complexity of SAW systems and in each case used them advantageously, this work carefully examines the behaviour of particles in a TSAW field. In doing so, this study expounds the key features of a complex acoustic field resulting from diffraction patterns of a travelling SAW through a three-dimensional spatial system. The outcomes are discussed in terms of diffraction effects which lead to multiple distinct particle patterning behaviours in the propagation and lateral directions under the influence of ARF. Additionally, streaming effects occur both at the sides of the TSAW beam and within its extent. The relative influence of these effects are compared for high frequency acoustic beams produced by a series of finite-width interdigitated transducers (187.5  $\mu\text{m}$ , 375  $\mu\text{m}$ , 750  $\mu\text{m}$ , 1500  $\mu\text{m}$  wide), in channels of a range of dimensions (100  $\mu\text{m}$  and 200  $\mu\text{m}$  width and 26  $\mu\text{m}$ , 35  $\mu\text{m}$  and 46.5  $\mu\text{m}$  height) and increasing distances from the IDT (680  $\mu\text{m}$ , 1400  $\mu\text{m}$  and 2050  $\mu\text{m}$ ).

## 2 System mechanics

Application of an oscillating electrical signal to each electrode patterned on the piezoelectric substrate is used to generate substrate waves. An interdigitated transducer (IDT) is formed by patterning multiple electrodes in a periodic pattern dictated by the intended frequency of operation. Exciting the system at the synchronous frequency will result in each electrode's vibration to constructively interfere and generate a surface acoustic wave to propagate across the surface of the piezoelectric substrate. A TSAW couples into an overlying fluid in the form of a plane wave propagating at the Rayleigh angle  $\theta_R = \arcsin(c_0/c_s)$  where  $c_0$  and  $c_s$  represent the speed of sound in the liquid and the SAW phase velocity of the substrate, respectively. However, a complete description of the ensuing sound field must also consider the inherent diffraction of the waves. This is important in determining the spatial amplitude of the wavefront; this is true for both the SAW in the substrate and the wave coupled into the fluid. Diffraction can be accounted for by the Huygens-Fresnel principle.<sup>62</sup> This describes each vibrating point as a source of a spherical wavefront which interfere with each other, resulting in spatial amplitude variations. Typically, the impulse response of a system describes geometrically the arrival of each wavefront from all source locations, which is then convolved with the actual excitation waveform.<sup>62,63</sup> The locations in the sound field of maximum amplitude are those at which these secondary wave-

fronts constructively interfere. An alternative description, using a mathematical simplification, considers a source as consisting of an emitter of a plane wave and edge waves from the perimeter of the aperture.<sup>58,63</sup> These diffraction effects can strongly influence acoustic streaming and ARF, as these forces depend on the amplitude and gradient of the pressure field.

The acoustic radiation force acts directly on particles exposed to an ultrasonic field. For a particle radius much smaller than the acoustic wavelength ( $a \ll \lambda_{SAW}$ ) the time-averaged resultant radiation force is given by Eqn. 1,<sup>45,64</sup> derived using perturbation theory, considering continuity and the Navier-Stokes equation:

$$\mathbf{F}_{ARF} = -\pi a^3 \left[ \frac{2\kappa_0}{3} \Re [f_1^* P_1^* \nabla P_1] - \rho_0 \Re [f_2^* \mathbf{v}_1^* \cdot \nabla \mathbf{v}_1] \right] \quad (1)$$

where the asterisk indicates complex conjugates and  $\Re[\ ]$  the real part.  $P_1$  and  $\mathbf{v}_1$  are the first order pressure and velocity field and factors  $f_1$  and  $f_2$  are given by:

$$f_1 = 1 - \frac{\kappa_p}{\kappa_0} \quad (2a)$$

and

$$f_2 = \frac{2(1-\gamma)(\rho_p - \rho_0)}{2\rho_p + \rho_0(1-3\gamma)} \quad (2b)$$

where,

$$\gamma = -\frac{3}{2} \left[ 1 + i \left( 1 + \delta_v \right) \right] \tilde{\delta}_v \quad (2c)$$

$$\tilde{\delta}_v = \frac{\sqrt{2\eta}}{a\sqrt{\omega\rho_0}} \quad (2d)$$

$\kappa_0 = 1/(\rho_0 c_0^2)$  and  $\kappa_p$  denote the compressibility of the liquid and particle respectively,  $\rho_0$  and  $\rho_p$  represent density of liquid and particles respectively,  $\omega$  is the angular frequency of excitation and  $\eta$  is the shear viscosity coefficient of the fluid. As can be seen in Eqn. 1, both terms are a measure of the sound field (either pressure or fluid particle velocity) and the gradient of that term. The effect of taking the complex conjugate of these two terms means that the time variations, due to the oscillation of the harmonic sound field, are removed. Accordingly, the acoustic radiation force is a steady state force which acts to translate or capture particles over a much longer time scale than the time period of the excitation. The most common description of particle behaviour resulting from exposure to a travelling wave is migration in the direction of propagation. However, in this work, we will also investigate the role of diffraction in generating forces to trap particles in both lines parallel to the microfluidic channel edge (we term this parallel trapping) and into clumps along the channel length (orthogonal trapping), as depicted in Fig 1a.

An additional mechanism, acoustic streaming is a steady flow driven by Reynolds stresses. Reynolds stress is the body force, given in Eqn 3a,<sup>45,65</sup> that arises as a result of the time-averaged first-order acoustic momentum flux gradient. Acoustic streaming velocity,  $\mathbf{v}_2$  is obtained by equating the Reynolds stress to the time-averaged second order terms given in Eqn 3b.<sup>45,65</sup> Acoustic streaming in turn induces a drag force on a suspended particle that affects particle migration behaviour. For a spherical particle,

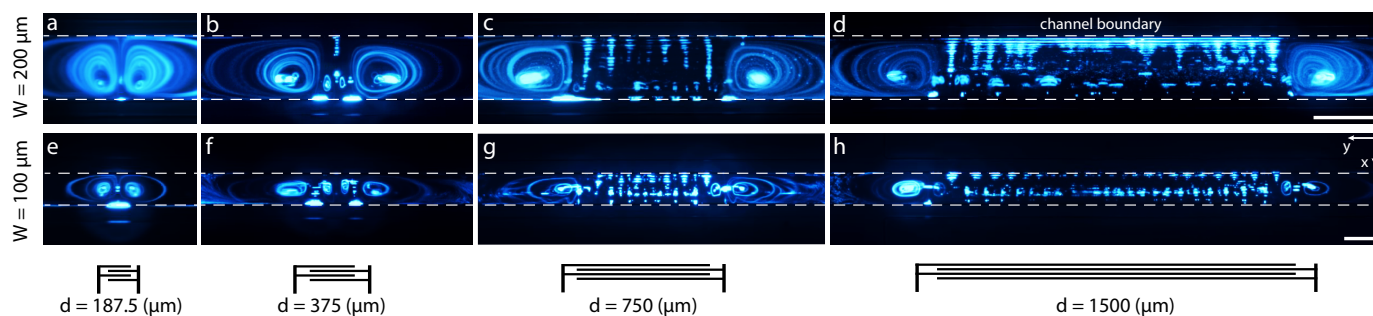


**Fig. 2** Experimental results of cross-over between streaming dominated to acoustic radiation dominated migration of (1  $\mu\text{m}$ ) particles, corresponding to distinct IDT apertures ( $d$ ) as well as channel widths ( $W$ ). 21  $\mu\text{m}$  wavelength TSAW (at 180 MHz frequency and 15 dBm generator power level) vary in their aperture sizes. Peripheral streaming dominated translation of particles is visualized in Figs (a-b) and (e-f). In between the peripheral streaming, ARF dominates and orthogonal as well as parallel trapping occurs as visualized in systems driven by 1500  $\mu\text{m}$  (d & h) and 750  $\mu\text{m}$  (c & g) aperture IDTs. All channels have a dimension  $H = 35 \mu\text{m}$  high. Scale bar is 200  $\mu\text{m}$  in (a-d) and 100  $\mu\text{m}$  in (e-h)

this is governed by the Stokes drag equation (Eqn 3c).

$$\langle \mathbf{F} \rangle = \rho_0 \langle (\mathbf{v}_1 \cdot \nabla) \mathbf{v}_1 + \mathbf{v}_1 \nabla \cdot \mathbf{v}_1 \rangle \quad (3a)$$

$$\langle \mathbf{F} \rangle = -\nabla \langle P_2 \rangle + \left[ \eta' + \left( \frac{4}{3} \right) \eta \right] \nabla (\nabla \cdot \mathbf{v}_2) + \eta \nabla^2 \mathbf{v}_2 \quad (3b)$$

$$\mathbf{F}_{drag} = 6\pi\eta a(\mathbf{v}_2 - \mathbf{v}_p) \quad (3c)$$

Where  $P_2$  and  $\mathbf{v}_2$  are the second-order (steady state) pressure and velocity field respectively.  $\eta'$  represents the bulk viscosity coefficient and  $\mathbf{v}_p$  is particle's velocity. Again, as with the acoustic radiation force, the time-averaged force magnitude scales with the spatial gradient of the pressure and velocity fields.

In this work, the excitation of a travelling wave gives rise to a steady swirling flow at the periphery of the finite-width SAW beam due to the large velocity gradient at this location in the width ( $x$ ) direction (which we term peripheral streaming). In addition, due to the diffraction lobes in the plane orthogonal to the electrodes ( $x$ - $z$  plane), a significant swirling motion is observed within the aperture of the IDT. These vortices occur about an axis parallel to the channel length (lobe streaming). These streaming based mechanisms are also depicted in Fig. 1a. Here, we examine the interactions of particles with a combined influence of ARF and streaming in a travelling wave system and how the relative influence of the effects depend on channel geometry, channel position and actuation power. This excitation gives rise to five distinct acoustofluidic actuation mechanisms beyond the standard propagation driven migration (Fig. 1a); an example of the results of streaming and ARF is shown in Fig. 1b. Fig. 1c depicts the streaming-driven vortices.

### 3 Methods

The device used in this work consists of a narrow microfluidic channel which is bonded onto a piezoelectric SAW device as shown in Fig. 1d. SAWs are produced using a straight interdigital transducer (IDT) designed with sets of 19, 14, 9, and 7 connected metallic finger pairs with overlapping width (aperture) of 187.5  $\mu\text{m}$ , 375  $\mu\text{m}$ , 750  $\mu\text{m}$  and 1500  $\mu\text{m}$  respectively. The IDT,

with 21  $\mu\text{m}$  pitch (operating at 180 MHz), are composed of a conductive 200 nm aluminium layer on top of a chromium adhesion layer deposited on a piezoelectric 128° rotated Y-cut X propagating Lithium Niobate (LiNbO<sub>3</sub>; LN) substrate using an e-beam evaporator. A 270 nm thick layer of SiO<sub>2</sub> was then deposited to insulate the electrodes from corrosion and to promote PDMS-LN

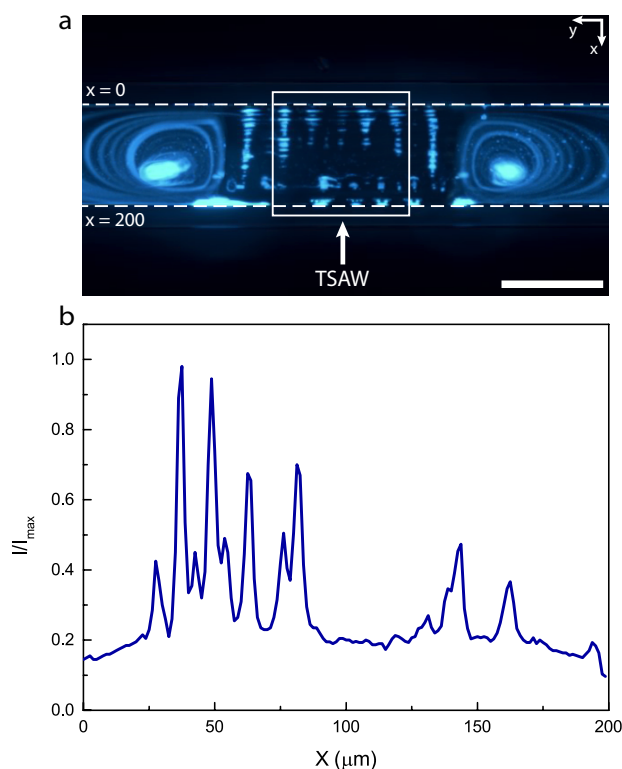


**Fig. 3** Travelling SAW results in particle migration in the propagation direction. (a) Experimental visualisation of 1  $\mu\text{m}$  particle behaviour existing within a channel ( $H = 35 \mu\text{m}$ ,  $W = 200 \mu\text{m}$ ), as a 21  $\mu\text{m}$  wavelength TSAW (at 180 MHz frequency and 15 dBm generator power level) interacts with the particles. (b) Normalized mean image intensity along the  $x$  direction of the area bounded within the white square in (a) as a function of  $x$  location indicating that most particles are located away from the IDT, i.e. as we move from  $x = 200 \mu\text{m}$  towards  $x = 0$ , showing that particles are displaced in the direction of TSAW propagation. Scale bar is 200  $\mu\text{m}$ .

bonding.

The experiments used a quiescent homogenous solution of fluorescent 1  $\mu\text{m}$  polystyrene particles (Magsphere, Pasadena, CA, USA) and water diluted with 0.2 % polyethylene glycol (PEG), which filled the rectangular microfluidic channel. To study the influence of channel geometry on the streaming flows and particle patterning within the system, 100  $\mu\text{m}$  and 200  $\mu\text{m}$  wide (along  $x$ -direction, see Fig. 1a) and 26  $\mu\text{m}$ , 35  $\mu\text{m}$  and 45.6  $\mu\text{m}$  high (along  $z$ -direction) microfluidic channels casted in polydimethylsiloxane (PDMS, 1:10 ratio of curing agent/polymer) were utilized. Upon application of an AC signal using a signal generator (Rohde and Schwarz HAMEG HM8134-3), particle behaviour was visualized via a fluorescence microscope (Olympus BX43) coupled with compatible light source (Olympus URFL-T). A PixeLink (PL-B782U usb2) CCD colour camera was used to capture the migration behaviour digitally. All spatial 2D measurements of particle collection were conducted via image intensity analysis using MATLAB.

To further investigate the effects of the system, a simplified 2-

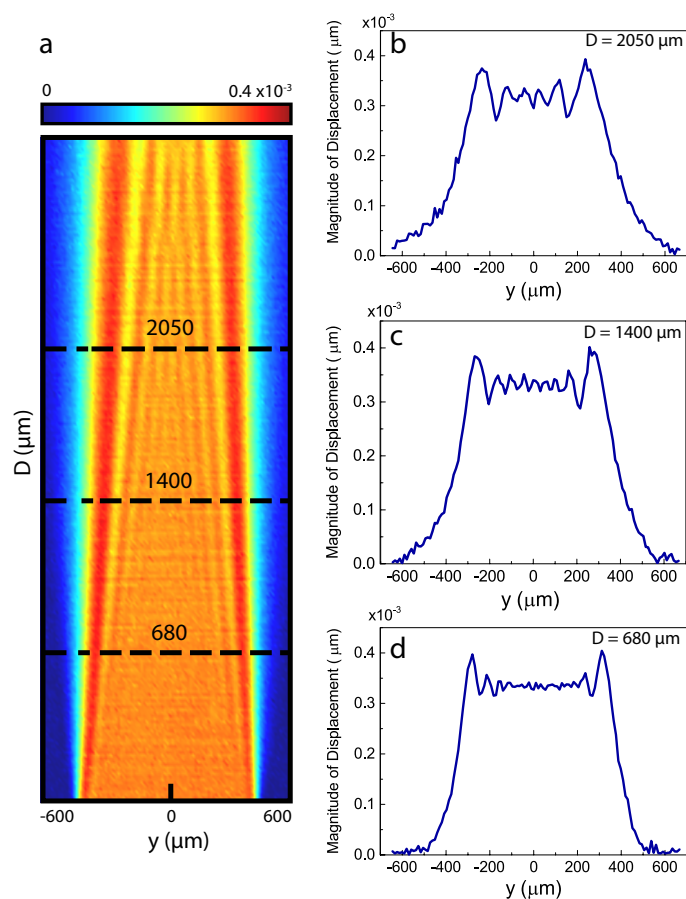


**Fig. 4** (a) Amplitude distribution of surface-normal displacement patterns on the LN substrate extending across IDT aperture measured via Laser Doppler vibrometer (LDV). An IDT (consisting of 7 finger pairs) with  $d = 750 \mu\text{m}$  was used here. (operating at applied generator voltage = 2.5 V and the frequency = 180 MHz). Dashed lines represent distinct channel locations used experimentally. (b)-(d) magnitude of substrate-normal displacement as a function of  $y$  location. The displacement have unit of  $\mu\text{m}$ .

dimensional fully coupled LN substrate and a fluid domain was modelled using COMSOL Multiphysics v 5.1. The relevant LN substrate properties were rotated to accommodate for the particular crystal cut orientation used experimentally. The single set of IDT were represented by equipotential lines on the piezoelectric solid domain, mimicking the IDT patterns used in the experiments, excited with a harmonic voltage potential (using a coupled electrostatic module) oscillating at the frequency of operation. This was then fully coupled to the fluid domain, modelled using the thermoviscous set of equations (Thermoacoustic module within COMSOL Multiphysics) to accurately capture the pressure and velocity fluctuations. This approach is similar to that of previous publications<sup>44,45</sup> with the exception that an assumed input displacement/velocity profile is not needed, as the coupled solid LN substrate is present. The PDMS ceiling of the fluid domain was modelled using an impedance boundary condition (this assumes that the thickness of the PDMS cover exceeds the attenuation length; as with the experimental device). However, the PDMS side walls were modelled with a coupled acoustic pressure domain consisting of a PDMS block 50  $\mu\text{m}$  wide on either side (similar to that of the PDMS wall thickness in experiments). The floor of the PDMS blocks were coupled to the solid LN substrate, which allows for the SAW displacement amplitude decay as well as any effects that arise due to the acoustic transmission through the PDMS wall into the fluid. There is no significant influence on the pressure field in the fluid domain arising from the pressure field in the PDMS block on either side, in line with observations reported by Collins *et al.*<sup>59,66</sup>

To obtain the second order streaming fields (i.e.  $v_2$ ), a laminar flow stationary study is carried out. The known first order velocity fields from the solved thermoviscous set of equations are utilised to calculate the body force (i.e. Reynold's stress) as in Eqn. 3a, which in turn is used to drive the fluid flow, resulting in the acoustic streaming fields. All the relevant parameters and properties used in the model are given in Table 1 provided in ESI.

## 4 Results and discussion

In a typical travelling wave system, whereby the wave is propagating orthogonally to a microfluidic channel and interacts with suspended matter (i.e. particles or droplets), the matters are pushed in the direction of wave propagation, conforming to present theoretical<sup>67</sup> and experimental literature. This effect has been used for sorting,<sup>68</sup> droplet displacement<sup>69</sup> and on-chip fluorescence-activated cell sorting (FACS).<sup>67,70,71</sup>

Similarly, we observe monodirectional translation of the particles, but our experiments show that it is one effect amongst many. When particles within a static aqueous solution are exposed to a finite-width TSAW beam they also experience acoustic radiation force due to the complex amplitude pattern caused by diffraction, as well as a drag force induced by acoustic streaming. The relative strength of these two forces, which varies spatially, dictates particle translation behaviour. As such, we describe a total of five distinct mechanisms that occur within a SAW system. These are, firstly, migration in the direction of TSAW propagation. Secondly, peripheral streaming, which consists of lateral streaming vortices at the vicinity of the SAW beam ( $x$ - $y$  plane). These extend across

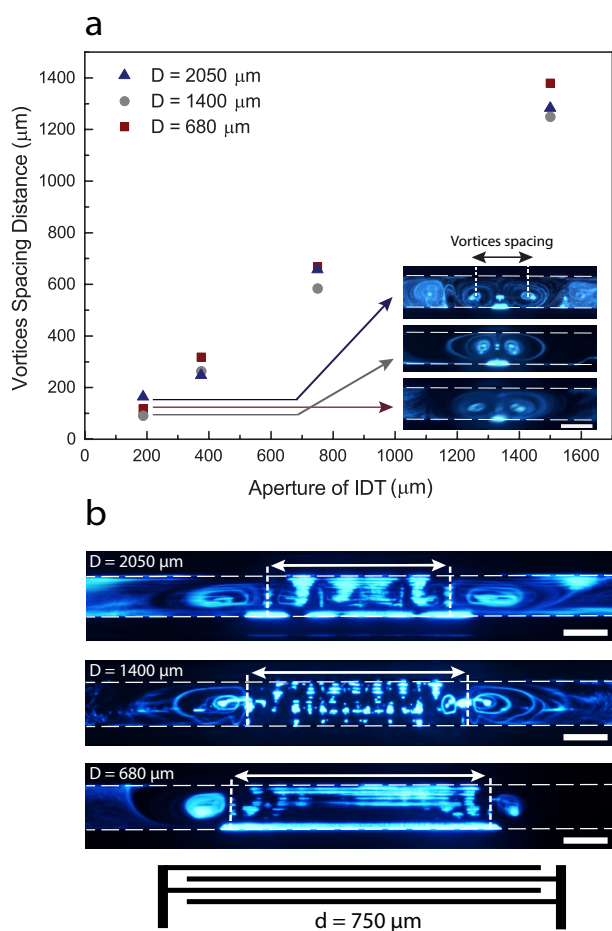


**Fig. 5** (a) Spacing between the center of each peripheral vortex for four different IDT aperture ( $d$ ) and three different channel locations ( $D$ ). The experimental images from (a) 187.5 μm and (b) 750 μm IDT are presented. (b) The spacing between inner edge of the peripheral vortices (shown with a double arrow between dashed lines) are 573 μm 468.6 μm and 428.3 μm for  $D$  of 680 μm, 1400 μm and 2050 μm respectively. Scale bar is 100 μm.

the entire width of the microfluidic channel ( $x$ -direction). Thirdly, lobe streaming which causes vertical vortices ( $x$ - $z$  plane) along the channel length ( $y$ -direction). These occur at the channel edge closest to the SAW-beam source and (in our experiments) are at a much smaller length scale compared to peripheral streaming. Fourthly, orthogonal trapping which creates particle aggregation in clumps along the length of channel ( $y$ -direction), and finally, parallel trapping, which forms periodic particle patterning across the microfluidic channel width ( $x$ -direction).

Whereas previous numerical and experimental studies have focused on some of these mechanisms individually, here we capture all these effects simultaneously in a single experimental set up, as shown in Fig. 2. This allows us to examine the underlying mechanisms and the alteration in particle behaviour (corresponding to geometric parameters of transducers as well as the channel dimensions) in the following subsections.

#### 4.1 Propagation migration

The most commonly described effect of TSAW is the migration of particles in the direction of propagation. This has been very effectively used for sized-based particle separation.<sup>48,68,72</sup> Destgeer *et al*<sup>55</sup> describe an area of the channel, along the channel edge nearest the ultrasound source, in which this doesn't occur, which they term an anechoic corner. Our work will show that behaviour in this area is dominated by streaming (lobe streaming), however outside this area we see a rich range of particle behaviour.

Nonetheless, underlying this, we do see an increase in particle concentration at the channel edge furthest from the IDT, consistent with migration in the direction of wave propagation. Fig. 3 shows the fluorescence intensity measured across the width of the channel, clearly showing an increase in particle numbers away from the source. For this particle size, the intensity is periodic arising from an additional mechanisms that we have identified, however, if the channel width were increased this would diminish<sup>65</sup> and propagation migration would dominate.

#### 4.2 Peripheral streaming

At the edges of the ultrasonic beam, substantial lateral vortices (within the  $x$ - $y$  plane) occur. In this location, large spatial gradients in pressure can be expected which will generate significant body forces on the fluid, according to Eqn. 3a. These vortices have previously been used for nanoparticle manipulation,<sup>42,73,74</sup> making use of the tendency for particles to be diverted into inner rotating streamlines and eventually focus them at the centre of the swirling fluid. This feature can be seen at each end of the channel along the length direction (besides the IDT aperture) in Fig. 2, with the size of the vortex extending the full width of the channel.

The formation of the ultrasonic SAW beam occurs in the substrate, hence, a Laser Doppler Vibrometer (LDV) scan has been performed (scan resolution = 10.5 μm) to characterise the width of the beam emerging from a 750 μm wide IDT operated at 180 MHz frequency and 18 dBm generator power level with no channel attached. The resultant displacement field arises from diffraction effects within the substrate which occur because of the finite IDT aperture. Across the TSAW beam, the area of maximum amplitude is in front of the IDT, though its width varies with propagation distance. Within the beam there are regions of higher and lower displacement amplitudes. Fig. 4 shows line scan data at three distinct distances ( $D$ ) from the IDT. The distance between the peak displacements in the beam decreases with propagation distance.

Figure 5a shows the experimental data taken for four different aperture widths and 3 distinct channel locations along the SAW beam. In every case the distance between the centre of each peripheral vortex is measured. By defining vortical spacing as a function of IDT aperture with the slope of 0.9, (vortical spacing = 0.9 aperture), it can be seen that in each case the separation distance is smaller than the IDT width ( $x$ -axis), in line with the LDV data. However, the downside is that this measure combines information about where the edge of the vortex is with the size of the vortex. To better compare how the vortex location changes

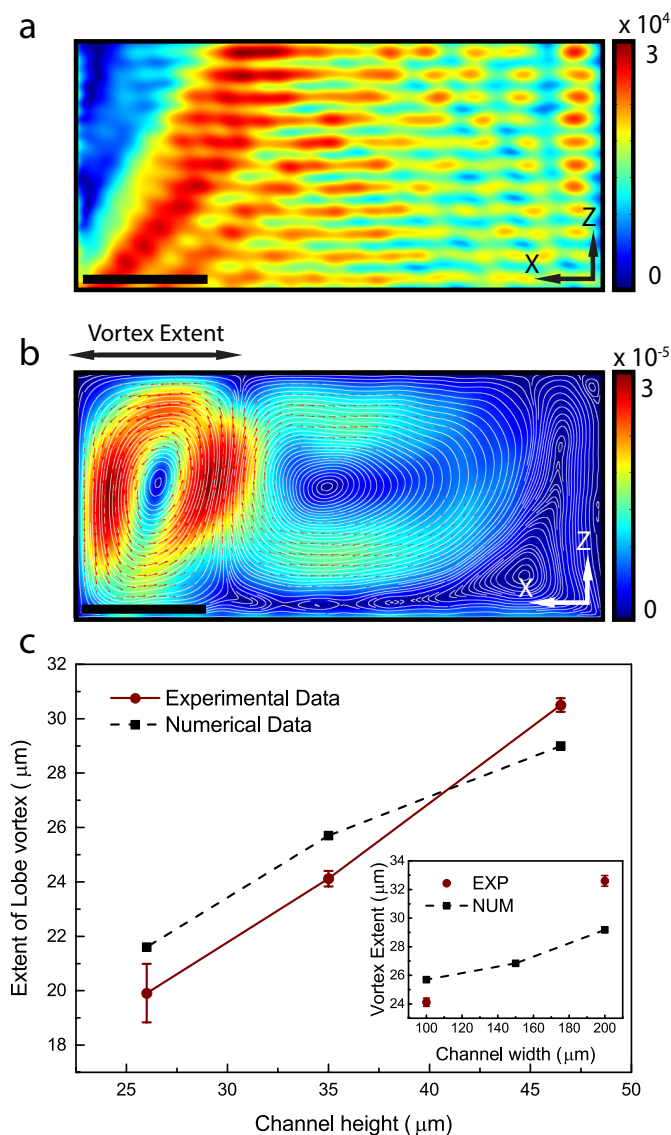


**Fig. 6** Surface plot for a 100  $\mu\text{m}$  wide, 46.5  $\mu\text{m}$  high channel of the (a) time-averaged absolute pressure field  $\langle |P| \rangle$  and (b) streamlines illustrating the simulated streaming field ( $\lambda_{\text{SAW}} = 21 \mu\text{m}$ ) along the channels' width. (c) Extent of the lobe streaming as a function of channel height  $H$  and width  $W$ . Numerical results (dashed lines) are compared with experimental results (solid lines). The error bars indicate standard error. Pressure and velocity surface plots have units of Pa and m/s respectively. Scale bars are 20  $\mu\text{m}$

with channel location, in Fig. 5b, the images from the 750  $\mu\text{m}$  IDT are presented and the distance between the inner edge of the vortices (extremity of the swirling flow) is measured, something which is more easily seen in the experimental videos. For larger propagation distances the vortex edges are closer together, measuring 573  $\mu\text{m}$ , 468  $\mu\text{m}$  and 428  $\mu\text{m}$  at propagation distances of 680  $\mu\text{m}$ , 1400  $\mu\text{m}$  and 2050  $\mu\text{m}$ , respectively. This is expected as observed from the narrowing beam seen in the LDV scan (Fig. 4), in which the separation between the two locations of maximum displacement on either side of the beam is 580  $\mu\text{m}$ , 537  $\mu\text{m}$  and 494  $\mu\text{m}$ . The relationship between the separation between peaks in the displacement field and the edges of the resulting vortices is

complicated by the complex link between body force generation, the resulting fluid motion and by the omission of a channel in the LDV scan. However, it is clear that the vortex separation is somewhat smaller than the peak to peak beam width, as expected.

### 4.3 Lobe streaming

Within the area between the two lateral vortices, some particles are influenced predominately by ARF and others by acoustic streaming induced drag forces, this spatial variation in which mechanism is dominant was shown by Devendran *et al*<sup>45</sup> for a SSW system, and is similarly observed here. Within this region we observe a vortex near the channel edge that occurs in the x-z plane.

The result of our numerical model, Fig. 6a, considers the absolute pressure field in a plane across the channel width (x-z plane with reference to Fig. 1a). As such it captures the diffraction which occurs in the fluid. The “anechoic corner”<sup>55,56</sup> an area of low pressure at the channel edge closest to the IDT, can be seen. The diffraction lobes which are formed, are present as areas of high pressure, the first of which occurs at approximately the Rayleigh angle and marks the boundary of the anechoic corner. In this region, the 1  $\mu\text{m}$  particles follow the fluid streamlines. Fig. 6b shows the predicted flow field in this plane, and shows a streaming vortex within the anechoic corner. As the lobe streaming vortex is driven by the first diffraction lobe, emerging from the substrate at an angle close to the Rayleigh angle, a change in channel height can be expected to change the extent of the vortex in an approximately linear manner. Fig. 6c, which compares simulation and experimental data, shows that this is indeed the case. In addition, the data (Fig. 6c inset) demonstrates that an increase in channel width also increases the extent of the vertical vortex. From Fig. 6b, it can be seen that the lobe vortex drives a weaker vortex across the rest of the channel width, where an increase in channel width results in a weakened secondary vortex. This, in turn, allows the lobe vortex to grow in size. This increase in size is, however, small compared to the increase in channel width, indicating that at larger widths there is considerably more channel area, in which streaming is not dominant.

### 4.4 Orthogonal trapping

It is only in areas which are less influenced by streaming that particle patterning can be observed. This occurs between the two peripheral streaming vortices and beyond the extent of the lobe vortex, it is in this region that ARF dominates. These patterns can be seen in Fig. 2, for the two wider IDT widths (750  $\mu\text{m}$  and 1500  $\mu\text{m}$ ). The particles' location is dictated by radiation forces acting in both the x and y-directions. Such patterns occur due to diffraction of the TSAW in both the substrate and the fluid. We examine the formation of these patterns in two stages, firstly dealing with the periodic clustering along the length of the channel (orthogonal trapping), and then subsequently examining the periodicity across the channel width (parallel trapping). Whilst the spacing between the peripheral streaming vortices is related to the width of the SAW beam as it diffracts in the substrate, orthogonal trapping is caused by finer details within the diffraction pattern. It

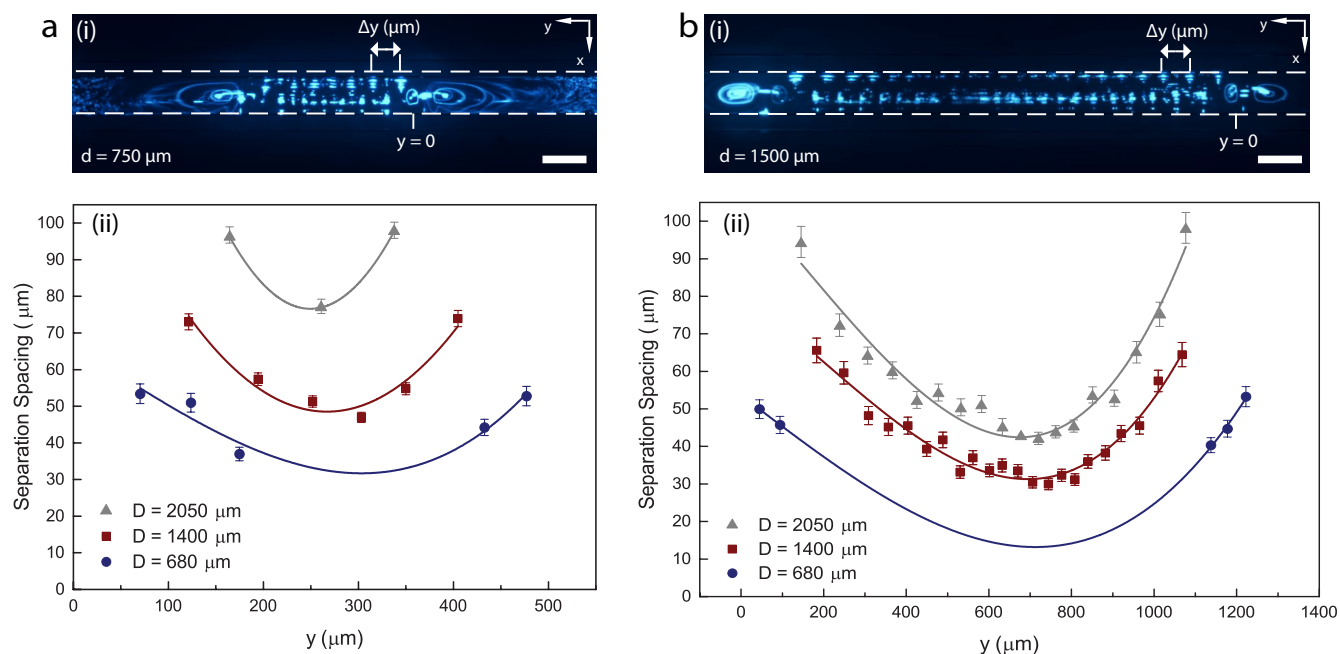


**Fig. 7** Spacing of particle aggregation as a function of  $y$  locations with  $y = 0$  corresponding to the rightmost approximated edge of the SAW-beam. Experimental results for three distinct channel/IDT distances ( $D$ ) shown for devices, each consisting of an IDT with (a)  $d = 750 \mu\text{m}$  and (b)  $d = 1500 \mu\text{m}$ . The error bars indicate standard error. Scale bar is  $100 \mu\text{m}$

can be seen from the LDV data in Fig. 4a that there are ripples in the displacement amplitudes across the width of the beam. This data is captured from a bare chip, thus, the diffraction causing these ripples is entirely on the substrate. Generally, in ultrasonic beamforming, the nearfield pressure amplitude (in a fluid bound wave) has a complex distribution of peaks and troughs arranged laterally across the beam width. For increasing distances from the IDT, these features remain present but diminish in quantity and the spacing tends to increase. Consider the width of the IDT to be a series of point sources, in line with Huygens-Fresnel principle; at a point in front of the aperture the distance to each of these point sources will differ, hence the phase of each wavelet is different. This governs the resulting amplitude at that location. If the point is further from the aperture, this difference in phase from each point source is smaller. The resulting features in the displacement field are therefore larger in size. These features can be seen more clearly in the line scans across the width of the beam (4b-d). It can be seen that for the line scan closer to the IDT that the features are indeed finer and more numerous. In addition, it can be seen that the inter-trough spacing is wider at each edge of the beam than in the middle.

In order to demonstrate that orthogonal trapping is due to substrate diffraction, we have examined the patterns formed using channels located at different distances from the IDT. Fig. 7 shows this data, with the spacing between clusters plotted against cluster location for three different channel locations and two IDT widths (the curves are fitted and intended simply to visually tie the relevant data points together). When comparing with the LDV measurement (Fig 4), we must bear in mind that these measurements are made in the absence of the channel, and that the mea-

surement plane is on the substrate surface and not in the fluid. Nonetheless, the trends match well. The experimental data shows that the spacing ( $\Delta Y$ ) between the particle clusters are larger at the edges of the beam, and that the feature spacings are larger when the channel is positioned further from the IDT. The variation in separation across the width of the IDT is clearly indicative that this is not simply a case of reflections causing a wave to be established along the length of the channel, as this would have yielded regularly spaced clustering.

#### 4.5 Parallel trapping

Particle clustering also takes place across the width of the channel. This is due to diffraction which occurs in the cross-sectional plane of the channel ( $x$ - $z$  plane in Fig. 1a). As the SAW couples into the microfluidic channel, its finite width acts as an aperture and diffraction ensues. As with the diffraction in the substrate, the geometry of the system dictates that the particles are within the near-field of the sound field, in this region lobes of maximum pressure occur. Devendran *et al*<sup>58</sup> showed that the diffraction in this plane can cause particle trapping across the width of the channel, though in their paper, this trapping was located at the edge of the channel closest to the IDT. In the systems studied here, the width of the channels are considerably smaller, so the effect stretches across the full width of the channel. However at the edge nearest the IDT these patterns are disturbed by the lobe vortex.

Figure 8 highlights the patterns and shows a model of the pressure field in this plane. The first pressure lobe is easily seen and occurs at approximately the Rayleigh angle. More careful inspection also reveals other lobes at lower angles which result in varia-

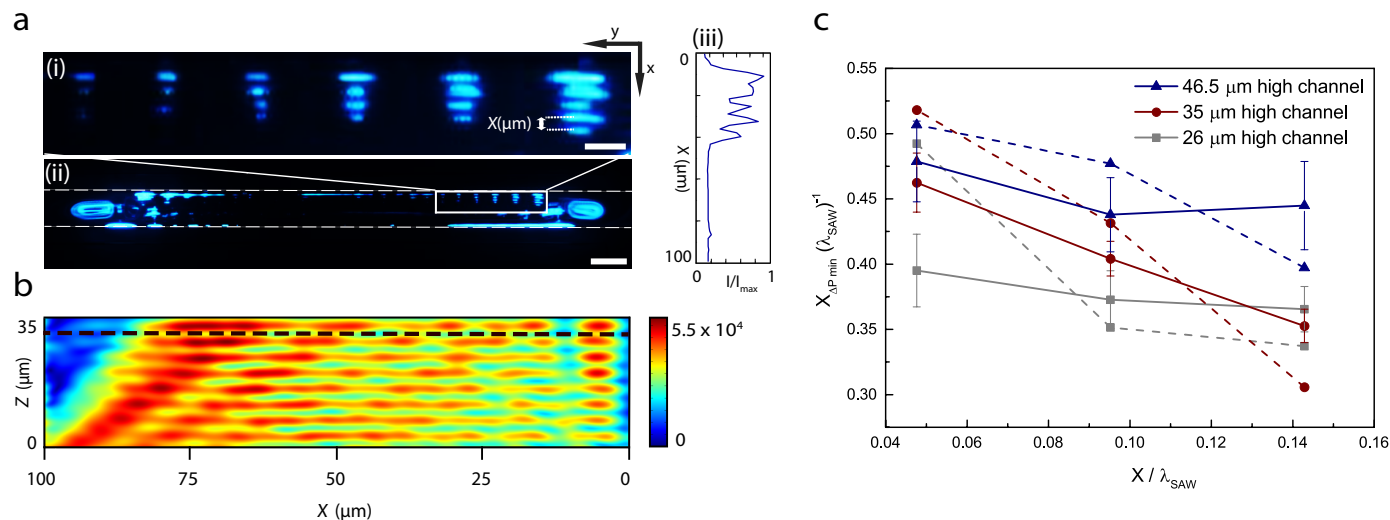


**Fig. 8** (a) Experimental results demonstrating the observed parallel trapping along channel width ( $W = 100 \mu\text{m}$ ,  $H = 35 \mu\text{m}$ ) driven by IDT ( $\lambda_{\text{SAW}} = 21 \mu\text{m}$ ,  $d = 1500 \mu\text{m}$ ). The image (i) is an inset of a particular section in (ii) bounded by the white rectangle. (iii) Peaks in  $y$ -averaged image intensity indicates particle alignment locations. (b) Numerical model depicting the first-order time-averaged absolute pressure field ( $\langle |P1| \rangle$ ) established within the channel. (c) The spacing between parallel trapping locations (in experimental observations represented with solid lines) as well as minimum pressure locations (numerical results for a  $W = 100 \mu\text{m}$ ,  $H = 35 \mu\text{m}$  channel shown in dashed lines) as a function of  $x$  locations, normalized by  $\lambda_{\text{SAW}}$ . The error bars indicate standard error. Pressure surface plot has unit of Pa. Scale bars are  $30 \mu\text{m}$  and  $100 \mu\text{m}$  in (a)(i) and (a)(ii) respectively.

tion in the amplitude of the absolute pressure across the width of the channel. Upon actuation, the particles are pushed along these structures in the sound field to the top of the channel where they are held in the local pressure minima. Due to the angled nature of these lobes, a higher channel will result in wider separation between the clusters, and likewise the structures nearest to the far wall should be separated by the greatest distances. Both these trends are seen in the experimental and simulation data shown in Fig. 8c, in which image intensities are analysed to precisely identify particle alignment positions across the channel's width. The spacing of the particles is plotted against the location of each set of particles in the  $x$  (opposite to propagation) direction with both distances normalized by the SAW wavelength. It should be noted that these features are not due to reflection of the fluid bound wave from the channel wall, firstly, this reflection is highly inefficient, an analysis of the acoustic impedance mismatch shows that only approximately 4% of the acoustic energy is reflected.<sup>70</sup> Secondly, if this were the case, the separation between the lines should be consistently  $0.5 \lambda_{\text{SAW}}$  regardless of channel width or height, not the case here.

The experimental images of particle behaviour have been used to identify five mechanisms. Of these, propagation migration is well understood and widely described in the literature. The analysis performed has allowed the other four mechanisms to be related to diffraction in the substrate (yielding peripheral streaming and orthogonal patterning) and in the fluid (yielding lobe streaming and parallel patterning).

## 5 Conclusion

In this study, we have experimentally investigated various phenomena arising from the incidence of a propagating finite-width SAW beam into an enclosed quiescent fluid. The Huygens-

Fresnel principle, wherein superposition of edge waves with planar waves yield rather complex diffraction patterns in the propagating TSAW is utilized to describe experimental findings, aided by numerical simulations. Acoustic radiation force arises from pressure field distributions in the fluid, with configurations significantly affected by diffraction effects in the propagating TSAW within the fluid and along fluid/LN interface. The resultant radiation force translates particles to the stabilised pressure minima locations despite the TSAW's continuous propagation. As such, distinct particle patterning along channel width and length parallel and orthogonal to the propagation direction are achieved respectively. In addition, streaming is observed in the form of large lateral vortices at the periphery regions of the ultrasonic beam, and a vertical vortex between the channel edge and first diffraction lobe. The cross over from streaming-dominated to radiation-dominated behaviour of particles depend on the geometries of IDT as well as that of the microfluidic channel. These findings and observations give rise to a better understanding of the underlying physics in SAW-driven technologies that can be achieved, which is essential in unlocking the full potential of such systems and introducing a broader range of applications.

## 6 Acknowledgements

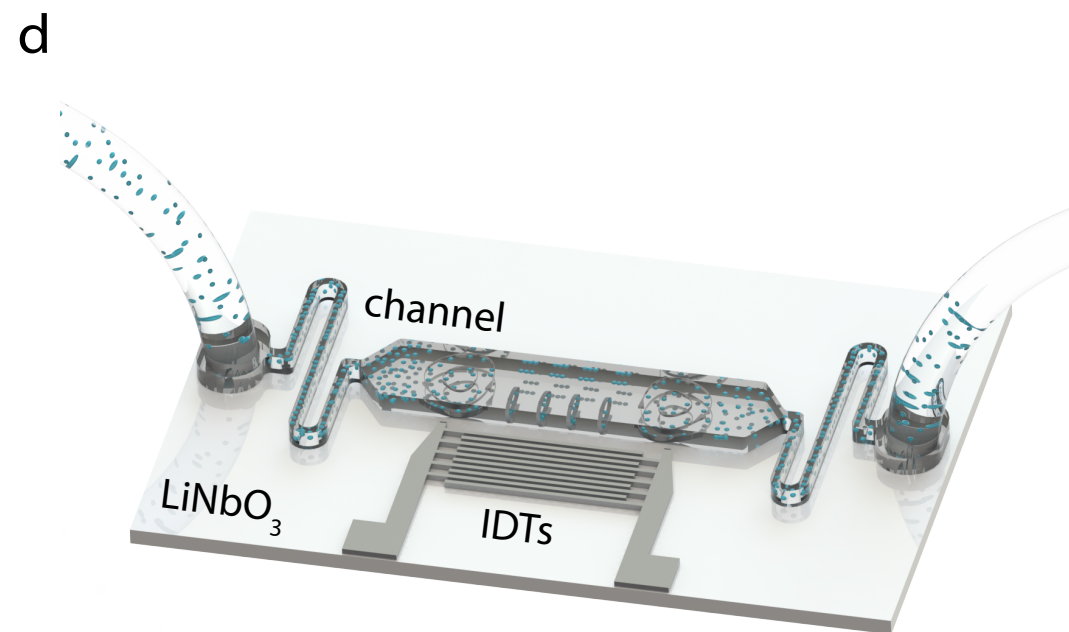
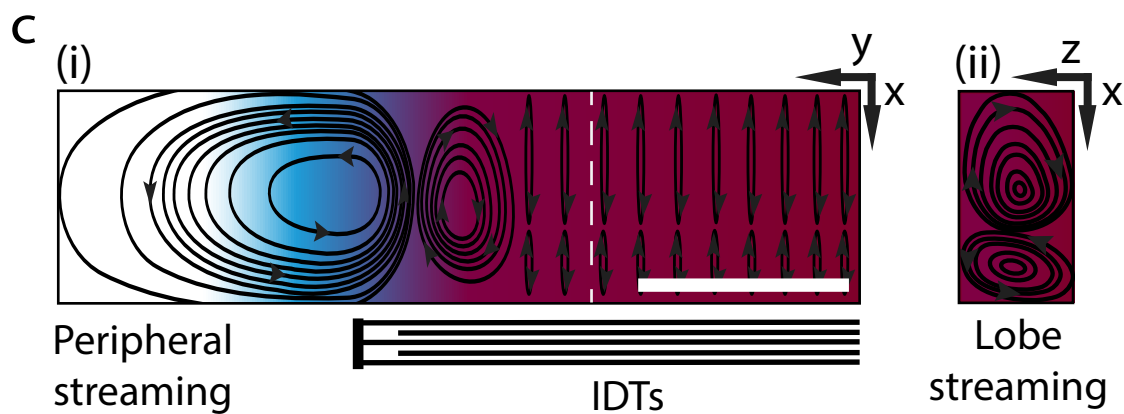
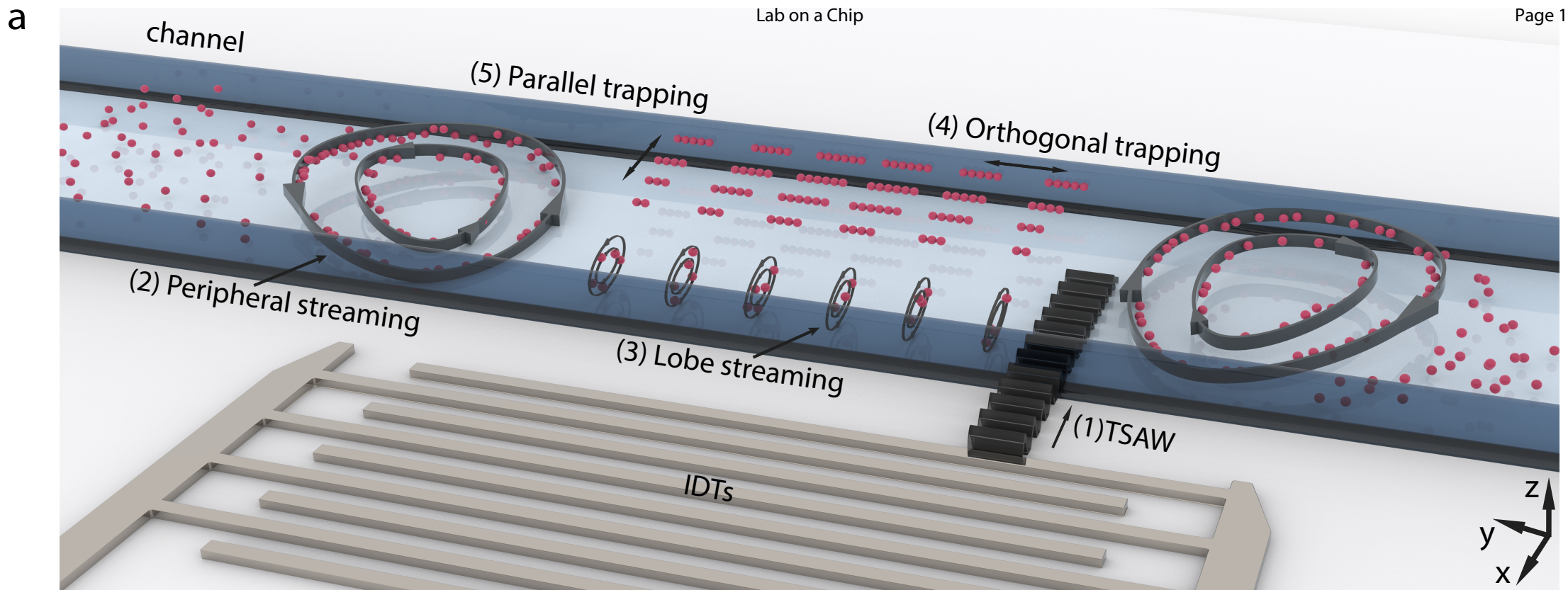
We gratefully acknowledge support received from the Australian Research Council, Grant No. DP160101263. All devices used in this work were fabricated at the Melbourne Centre for Nanofabrication (MCN). This research was undertaken with the assistance of resources from the National Computational Infrastructure (NCI), which is supported by the Australian Government.

## References

- 1 M. Fouet, M. A. Mader, S. Irain, Z. Yanha, A. Naillon, S. Carrou, A. M. Gue and P. Joseph, *Lab Chip*, 2016, **16**, 720–33.

- 2 K. He, S. T. Retterer, B. R. Srijanto, J. C. Conrad and R. Krishnamoorti, *ACS nano*, 2014, **8**, 4221–4227.
- 3 J. McGrath, M. Jimenez and H. Bridle, *Lab Chip*, 2014, **14**, 4139–58.
- 4 M. Yamada, M. Nakashima and M. Seki, *Analytical Chemistry*, 2004, **76**, 5465–5471.
- 5 Y. Wang, Y. Zhao and S. K. Cho, *Journal of Micromechanics and Microengineering*, 2007, **17**, 2148–2156.
- 6 N. Xia, T. P. Hunt, B. T. Mayers, E. Alsberg, G. M. Whitesides, R. M. Westervelt and D. E. Ingber, *Biomed Microdevices*, 2006, **8**, 299–308.
- 7 P. R. Gascoyne and J. Vykoukal, *Electrophoresis*, 2002, **23**, 1973.
- 8 H. Shafiee, M. B. Sano, E. A. Henslee, J. L. Caldwell and R. V. Davalos, *Lab Chip*, 2010, **10**, 438–45.
- 9 B. Landenberger, H. Hofemann, S. Wadle and A. Rohrbach, *Lab Chip*, 2012, **12**, 3177–83.
- 10 H. F. Levison and A. Morbidelli, *Nature*, 2003, **426**, 419–21.
- 11 X. Ding, S.-C. S. Lin, B. Kiraly, H. Yue, S. Li, I.-K. Chiang, J. Shi, S. J. Benkovic and T. J. Huang, *Proceedings of the National Academy of Sciences*, 2012, **109**, 11105–11109.
- 12 M. Wiklund, *Lab Chip*, 2012, **12**, 2018–28.
- 13 D. Bazou, R. Kearney, F. Mansergh, C. Bourdon, J. Farrar and M. Wride, *Ultrasound Med Biol*, 2011, **37**, 321–30.
- 14 J. Hultstrom, O. Manneberg, K. Dopf, H. M. Hertz, H. Brismar and M. Wiklund, *Ultrasound Med Biol*, 2007, **33**, 145–51.
- 15 N. Sivanantha, C. Ma, D. J. Collins, M. Sesen, J. Brenker, R. L. Coppel, A. Neild and T. Alan, *Applied Physics Letters*, 2014, **105**, 103704.
- 16 A. Haake, A. Neild, G. Radziwill and J. Dual, *Biotechnology and Bioengineering*, 2005, **92**, 8–14.
- 17 M. Hill, Y. Shen and J. J. Hawkes, *Ultrasonics*, 2002, **40**, 385–392.
- 18 M. Hill and R. J. Wood, *Ultrasonics*, 2000, **38**, 662–665.
- 19 X. Ding, P. Li, S.-C. S. Lin, Z. S. Stratton, N. Nama, F. Guo, D. Slotcavage, X. Mao, J. Shi and F. Costanzo, *Lab Chip*, 2013, **13**, 3626–3649.
- 20 V. Skowronek, R. W. Rambach, L. Schmid, K. Haase and T. Franke, *Analytical Chemistry*, 2013, **85**, 9955–9959.
- 21 L. Y. Yeo and J. R. Friend, *Biomechanics*, 2009, **3**, 012002.
- 22 S.-C. S. Lin, X. Mao and T. J. Huang, *Lab Chip*, 2012, **12**, 2766–2770.
- 23 T. Laurell, F. Petersson and A. Nilsson, *Chemical Society Reviews*, 2007, **36**, 492–506.
- 24 I. Leibacher, P. Reichert and J. Dual, *Lab Chip*, 2015, **15**, 2896–2905.
- 25 I. Leibacher, S. Schatzer and J. Dual, *Lab Chip*, 2014, **14**, 463–470.
- 26 G. Vuillermet, P.-Y. Gires, F. Casset and C. Poulain, *Physical Review Letters*, 2016, **116**, 184501.
- 27 G. Destgeer, K. H. Lee, J. H. Jung, A. Alazzam and H. J. Sung, *Lab Chip*, 2013, **13**, 4210–4216.
- 28 F. Guo, Z. Mao, Y. Chen, Z. Xie, J. P. Lata, P. Li, L. Ren, J. Liu, J. Yang, M. Dao et al., *Proceedings of the National Academy of Sciences*, 2016, **113**, 1522–1527.
- 29 M. Wu, Y. Ouyang, Z. Wang, R. Zhang, P.-H. Huang, C. Chen, H. Li, P. Li, D. Quinn, M. Dao et al., *Proceedings of the National Academy of Sciences*, 2017, **114**, 10584–10589.
- 30 J. C. Brenker, D. J. Collins, H. Van Phan, T. Alan and A. Neild, *Lab Chip*, 2016, **16**, 1675–1683.
- 31 M. Sesen, T. Alan and A. Neild, *Lab Chip*, 2014, **14**, 3325–33.
- 32 L. Schmid and T. Franke, *Applied Physics Letters*, 2014, **104**, 133501.
- 33 M. Sesen, C. Devendran, S. Malikides, T. Alan and A. Neild, *Lab Chip*, 2017, **17**, 438–447.
- 34 S. R. Heron, R. Wilson, S. A. Shaffer, D. R. Goodlett and J. M. Cooper, *Analytical Chemistry*, 2010, **82**, 3985–3989.
- 35 A. Qi, L. Y. Yeo and J. R. Friend, *Physics of Fluids*, 2008, **20**, 074103.
- 36 D. J. Collins, B. Morahan, J. Garcia-Bustos, C. Doerig, M. Plebanski and A. Neild, *Nature Communications*, 2015, **6**, 8686.
- 37 J. Shi, D. Ahmed, X. Mao, S.-C. S. Lin, A. Lawit and T. J. Huang, *Lab Chip*, 2009, **9**, 2890–2895.
- 38 D. J. Collins, T. Alan and A. Neild, *Lab Chip*, 2014, **14**, 1595–1603.
- 39 J. Shi, H. Huang, Z. Stratton, Y. Huang and T. J. Huang, *Lab Chip*, 2009, **9**, 3354–3359.
- 40 C. Devendran, N. R. Gunasekara, D. J. Collins and A. Neild, *RSC Advances*, 2016, **6**, 5856–5864.
- 41 A. Fakhfour, C. Devendran, D. J. Collins, Y. Ai and A. Neild, *Lab Chip*, 2016, **16**, 3515–3523.
- 42 D. J. Collins, Z. Ma and Y. Ai, *Analytical Chemistry*, 2016, **88**, 5513–5522.
- 43 H. Bruus, *Journal of Fluid Mechanics*, 2017, **826**, 1–4.
- 44 P. B. Muller, R. Barnkob, M. J. H. Jensen and H. Bruus, *Lab Chip*, 2012, **12**, 4617–4627.
- 45 C. Devendran, T. Albrecht, J. Brenker, T. Alan and A. Neild, *Lab Chip*, 2016, **16**, 3756–3766.
- 46 C. Devendran, I. Gralinski and A. Neild, *Microfluidics and Nanofluidics*, 2014, **17**, 879–890.
- 47 H. Bruus, *Lab Chip*, 2012, **12**, 1014–21.
- 48 G. Destgeer, B. H. Ha, J. Park, J. H. Jung, A. Alazzam and H. J. Sung, *Physics Procedia*, 2015, **70**, 34–37.
- 49 J. Shi, X. Mao, D. Ahmed, A. Colletti and T. J. Huang, *Lab Chip*, 2008, **8**, 221–223.
- 50 C. Grenvall, P. Augustsson, J. R. Folkenberg and T. Laurell, *Analytical Chemistry*, 2009, **81**, 6195–6200.
- 51 J. Dual, P. Hahn, I. Leibacher, D. Möller, T. Schwarz and J. Wang, *Lab Chip*, 2012, **12**, 4010–4021.
- 52 J. Lei, P. Glynn-Jones and M. Hill, *Lab Chip*, 2013, **13**, 2133–2143.
- 53 P. B. Muller, M. Rossi, Á. Marín, R. Barnkob, P. Augustsson, T. Laurell, C. J. Kaehler and H. Bruus, *Physical Review E*, 2013, **88**, 023006.
- 54 A. Neild, S. Oberti, A. Haake and J. Dual, *Ultrasonics*, 2006, **44**, e455–e460.
- 55 G. Destgeer, B. H. Ha, J. Park, J. H. Jung, A. Alazzam and H. J.

- Sung, *Analytical Chemistry*, 2015, **87**, 4627–4632.
- 56 F. Kiebert, S. Wege, J. Massing, J. König, C. Cierpka, R. Weser and H. Schmidt, *Lab Chip*, 2017, **17**, 2104–2114.
- 57 G. Destgeer, A. Alam, H. Ahmed, J. Park, J. H. Jung, K. Park and H. J. Sung, *Applied Physics Letters*, 2018, **112**, 083501.
- 58 C. Devendran, D. J. Collins, Y. Ai and A. Neild, *Physical Review Letters*, 2017, **118**, 154501.
- 59 D. J. Collins, R. O'Rorke, C. Devendran, Z. Ma, J. Han, A. Neild and Y. Ai, *Physical Review Letters*, 2018, **120**, 074502.
- 60 J. W. Ng, C. Devendran and A. Neild, *Lab Chip*, 2017, **17**, 3489–3497.
- 61 J. W. Ng, D. J. Collins, C. Devendran, Y. Ai and A. Neild, *Microfluidics and Nanofluidics*, 2016, **20**, 151.
- 62 S.-C. Wooh and Y. Shi, *Journal of Nondestructive Evaluation*, 1999, **18**, 39–57.
- 63 H. G. Kraus, *Journal of the Optical Society of America A*, 1989, **6**, 1196–1205.
- 64 M. Settnes and H. Bruus, *Physical Review E*, 2012, **85**, 016327.
- 65 W. L. M. Nyborg, *Physical Acoustics*, Elsevier, 1965, vol. 2, pp. 265–331.
- 66 D. J. Collins, C. Devendran, Z. Ma, J. W. Ng, A. Neild and Y. Ai, *Science Advances*, 2016, **2**, e1600089.
- 67 Z. Zhu and C. J. Yang, *Accounts of Chemical Research*, 2016, **50**, 22–31.
- 68 G. Destgeer, B. H. Ha, J. H. Jung and H. J. Sung, *Lab Chip*, 2014, **14**, 4665–4672.
- 69 T. Franke, A. R. Abate, D. A. Weitz and A. Wixforth, *Lab Chip*, 2009, **9**, 2625–2627.
- 70 D. J. Collins, A. Neild and Y. Ai, *Lab Chip*, 2016, **16**, 471–479.
- 71 X. Ding, S.-C. S. Lin, M. I. Lapsley, S. Li, X. Guo, C. Y. Chan, I.-K. Chiang, L. Wang, J. P. McCoy and T. J. Huang, *Lab Chip*, 2012, **12**, 4228–4231.
- 72 W. Ung, K. Mutafooulos, P. Spink, R. W. Rambach, T. Franke and D. A. Weitz, *Lab Chip*, 2017, **17**, 4059–4069.
- 73 D. J. Collins, Z. Ma, J. Han and Y. Ai, *Lab Chip*, 2017, **17**, 91–103.
- 74 D. J. Collins, B. L. Khoo, Z. Ma, A. Winkler, R. Weser, H. Schmidt, J. Han and Y. Ai, *Lab Chip*, 2017, **17**, 1769–1777.



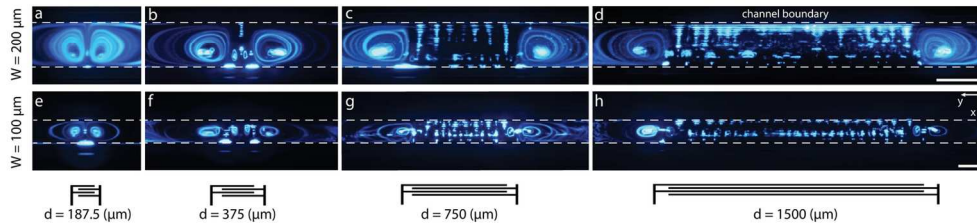
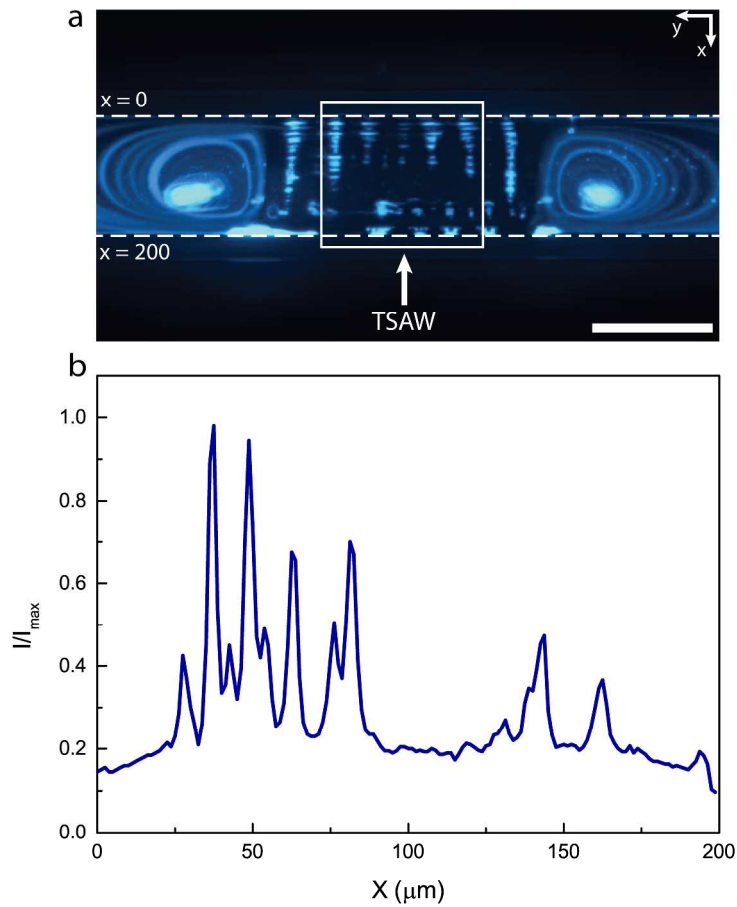


Fig. 2 Experimental results of cross-over between streaming dominated to acoustic radiation dominated migration of (1  $\mu\text{m}$ ) particles, corresponding to distinct IDT apertures ( $d$ ) as well as channel widths ( $W$ ). 21  $\mu\text{m}$  wavelength TSAW (at 180 MHz frequency and 15 dBm generator power level) vary in their aperture sizes. Peripheral streaming dominated translation of particles is visualized in Figs (a-b) and (e-f). In between the peripheral streaming, ARF dominates and orthogonal as well as parallel trapping occurs as visualized in systems driven by 1500  $\mu\text{m}$  ( $d$  &  $h$ ) and 750  $\mu\text{m}$  ( $c$  &  $g$ ) aperture IDTs. All channels have a dimension  $H = 35 \mu\text{m}$  high. Scale bar is 200  $\mu\text{m}$  in (a-d) and 100  $\mu\text{m}$  in (e-h)

139x44mm (300 x 300 DPI)



Travelling SAW results in particle migration in the propagation direction. (a) Experimental visualisation of 1  $\mu\text{m}$  particle behaviour existing within a channel ( $H = 35 \mu\text{m}$ ,  $W = 200 \mu\text{m}$ ), as a 21  $\mu\text{m}$  wavelength TSAW (at 180 MHz frequency and 15 dBm generator power level) interacts with the particles. (b) Normalized mean image intensity along the x direction of the area bounded within the white square in (a) as a function of x location indicating that most particles are located away from the IDT, i.e. as we move from  $x = 200 \mu\text{m}$  towards  $x = 0$ , showing that particles are displaced in the direction of TSAW propagation. Scale bar is 200  $\mu\text{m}$ .

297x278mm (300 x 300 DPI)

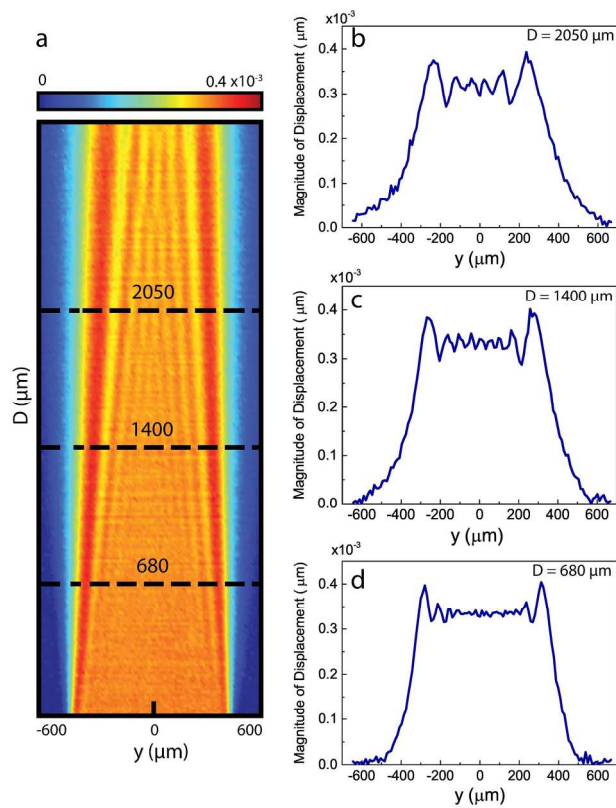


Fig. 4 (a) Amplitude distribution of surface-normal displacement patterns on the LN substrate extending across IDT aperture measured via Laser Doppler vibrometer (LDV). An IDT (consisting of 7 finger pairs) with  $d = 750 \mu\text{m}$  was used here. (operating at applied generator voltage = 2.5 V and the frequency = 180 MHz). Dashed lines represent distinct channel locations used experimentally. (b)-(d) magnitude of substratenormal displacement as a function of  $y$  location. The displacement have unit of  $\mu\text{m}$ .

192x158mm (300 x 300 DPI)

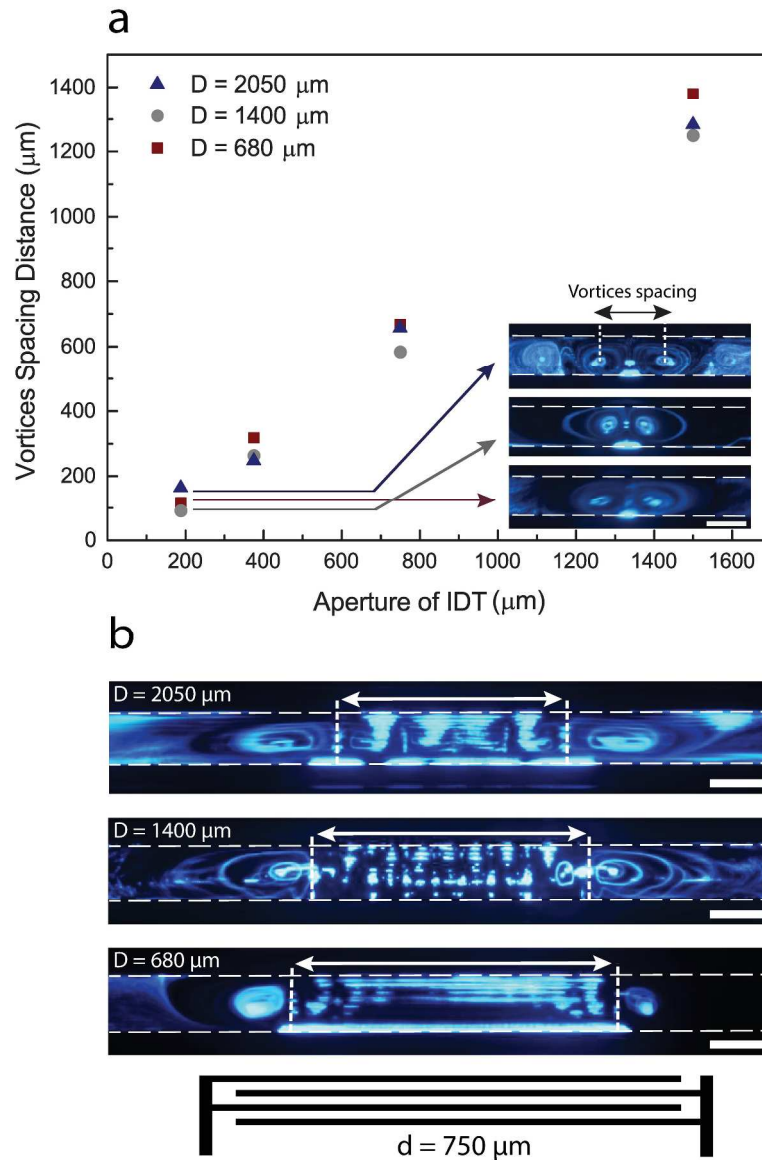


Fig. 5 (a) Spacing between the center of each peripheral vortex for four different IDT aperture ( $d$ ) and three different channel locations ( $D$ ). The experimental images from (a) 187.5  $\mu\text{m}$  and (b) 750  $\mu\text{m}$  IDT are presented.

(b) The spacing between inner edge of the peripheral vortices (shown with a double arrow between dashed lines) are 573  $\mu\text{m}$  468.6  $\mu\text{m}$  and 428.3  $\mu\text{m}$  for  $D$  of 680  $\mu\text{m}$ , 1400  $\mu\text{m}$  and 2050  $\mu\text{m}$  respectively. Scale bar is 100  $\mu\text{m}$ .

267x399mm (300 x 300 DPI)

